Chuliá-Jordán, R.; Santamaría Pérez, D.; Otero-De-La-Roza, A.; Ruiz-Fuertes, J.; Marqueño, T.; Gomis, O.; Macleod, S.... (2020). Phase Stability of Natural Ni0.75Mg0.22Ca0.03CO3 Gaspeite Mineral at High Pressure and Temperature. The Journal of Physical Chemistry C. 124(36):19781-19792. https://doi.org/10.1021/acs.jpcc.0c04509

Phase stability of natural $Ni_{0.75}Mg_{0.22}Ca_{0.03}CO_3$ gaspeite mineral at high pressure and temperature

R. Chuliá-Jordán[1], D. Santamaria-Perez[1,*], A. Otero-de-la-Roza[2], J. Ruiz-Fuertes[3], Tomas Marqueño[1], O Gomis[4], Simon MacLeod[5,6], Catalin Popescu[7].

[1] *Departamento de Física Aplicada-ICMUV, Universidad de Valencia, MALTA Consolider Team, Edificio de Investigación, C/Dr. Moliner 50, E-46100 Burjassot, Valencia, Spain.*

[2] *Departamento de Química Física y Analítica, Facultad de Química, Universidad de Oviedo, MALTA Consolider Team, E-33006 Oviedo, Spain*

[3] *DCITIMAC, Universidad de Cantabria, Avenida de Los Castros 48, 39005 Santander, Spain*

[4] *Centro de Tecnologías Físicas: Acústica, Materiales y Astrofísica, MALTA Consolider Team, Universitat Politècnica de València, 46022 València, Spain*

[5] *AWE, Aldermaston, Reading, RG7 4PR, UK*

[6] *SUPA, School of Physics and Astronomy, and Centre for Science at Extreme Conditions, The University of Edinburgh, Mayfield Road, Edinburgh EH9 3JZ, UK*

[7] *CELLS-ALBA Synchrotron Light Facility, 08290 Cerdanyola, Barcelona, Spain*

Abstract

Divalent metal carbonates play an important role in the Earth's carbon cycle, but the effect of chemical substitution is still poor known. In this work we have studied the structural and vibrational properties of natural mineral gaspeite ($Ni_{0.75}Mg_{0.22}Ca_{0.03}CO_3$) under high pressure and temperature using in situ synchrotron X-ray diffraction and Raman spectroscopy in diamond-anvil cells. These experiments have been complemented by *ab initio* simulations. Synchrotron high pressure XRD measurements at room temperature using He as pressure transmitting medium have shown that the calcite-type structure is stable up to 23.3 GPa. A bulk modulus at zero pressure of B_0 = 105(2) GPa with B_0' = 7.4(3) has been obtained from the experimental equation of state. This result indicates that gaspeite is the most incompressible of all the divalent metal carbonates. The axial compressibilities in gaspeite have a high anisotropy being the *c* axis about 3 times more compressible than the *a* axis. We have followed under pressure

the Raman modes of gaspeite up to 19 GPa. Moreover, $Ni_{0.75}Mg_{0.22}Ca_{0.03}CO_3$ compressed at 5.5 GPa has been heated up to 840 K, revealing that this carbonate is stable at those conditions. The equation of state of magnesian gaspeite at this temperature has been determined. Our *ab initio* calculations on $NiCO_3$ at zero pressure and 5.5 GPa have allowed us to estimate the thermal expansion coefficients. The obtained values show that the anisotropy in the thermal expansion is comparable to that found in axial compressibility.

Corresponding e-mail address: David.Santamaria@uv.es

Introduction

Carbonate minerals can be found in relatively large amounts in the Earth's crust. They form by weathering of silicate rocks and sedimentation processes. At convergent boundaries, a tectonic plate slides below another forming a subducting slab that sinks these carbonates into the mantle [1-2]. Experimental evidences shows that the redox state in the Earth mantle below 250 km depth transforms oxidized forms of carbon into reduced species such as diamond [3-4], but also that carbonates can be preserved in subducting slabs down to the lower mantle due to the sluggish kinetics of exchange reactions [5]. Super-deep diamonds have been reported to contain carbonate inclusions, suggesting the possible coexistence of reduced and oxidized species [6-7]. New experimental data on the high-pressure (HP) high-temperature (HT) stability of carbonate compounds is needed to better understand the Earth's carbon cycle [8-10].

Second and third row divalent metal carbonates mainly adopt the rhombohedral $R\bar{3}c$ calcite-type structure [11-12]. The simplicity of its atomic framework, consisting of rigid [CO_3] carbonate units whose oxygen atoms are corner-linked to slightly distorted metal-centered octahedra, makes it ideal to study compositional effects on the structure. For instance, the stability of the Mg and Ca calcite-type carbonates differs significantly under compression and heating. While $MgCO_3$ magnesite is stable throughout a wide pressure and temperature range (only one phase of $MgCO_3$ denser than magnesite has been found above 115 GPa and 2100–2200 K) [13], $CaCO_3$ calcite undergoes several HP phase transitions at relatively low pressures (six polymorphs at HP are known) [14-15]. There also exists two intermediate mineral phases in the $MgCO_3$-$CaCO_3$ system: $MgCa(CO_3)_2$ dolomite and $Mg_3Ca(CO_3)_4$ huntite, which behave differently under compression [16-17]. It seems clear that divalent metals with different radii and electronic characteristics present a distinctive behavior under compression. This is particularly relevant within the complex scenario of Earth's mantle, where natural compositions likely include several divalent cations coexisting with Mg^{2+}, which is thought to be the most abundant metal.

Despite the fact that the amount of divalent nickel metal in Earth's mantle is significant, there exist few studies of Ni-containing carbonates. The gaspeite mineral is defined as the nickel end-member of the $MgCO_3$-$NiCO_3$ solution

series [18]. However, pure naturally-occurring gaspeite has only been reported once [19], the rest of gaspeite specimens found are magnesian gaspeites or nickeloan magnesites [11, 18, 20], with general formula $Ni_xMg_{1-x}CO_3$. These solid solutions of intermediate compositions are metastable, likely formed at relatively low temperatures (below 373 K) in siliceous dolomite in the presence of nickel minerals, and they are thermodynamically unstable with respect to unmixing [21]. Pure $NiCO_3$ carbonate samples can be hydrothermally prepared in the laboratory [11, 22] but, as in nature, it was observed that the difficulty in synthesizing divalent carbonates increased with the degree of completeness in the filling of the d orbitals, from Mn to Ni [11]. Once formed, synthetic gaspeite is stable up to 553 K at ambient pressure. At higher temperature, it starts to decompose. Several decomposition temperatures at pressures in the 0-2.5 GPa range were reported, showing an approximate linear increase of decomposition temperatures with pressure at a rate of 160 K/GPa [11]. In other words, high pressure could prohibit gaspeite from decomposing at the high temperature associated with the geological formation environment. The role of pressure, temperature and nickel/magnesium substitution in the structural behavior of gaspeite carbonate remains to be understood.

The above considerations encouraged us to undertake a combined experimental and theoretical investigation of the structural behavior of magnesian gaspeite under HP and HT. Angle-dispersive X-ray diffraction (XRD) measurements have been complemented with theoretical *ab initio* calculations. The compressibility, axial anisotropy and thermal expansion for the calcite-type naturally-occurring $Ni_{0.75}Mg_{0.22}Ca_{0.03}CO_3$ phase are reported and discussed in relation to those of other carbonates. We also investigated theoretically the dependence of these parameters on the nickel to magnesium ratio, and subtle structural changes related to chemical composition.

Methods

Experimental details

A naturally-occurring magnesian gaspeite mineral specimen from the Kambalda, Western Australia locality was studied (Catalog number YPM-MIN-

041615, Mineralogy and Meteoritics Department, Yale Peabody Museum of Natural History). Light green magnesian gaspeite powder was carefully isolated, crushed with a mortar and pestle and characterized at ambient conditions by means of energy-dispersive x-ray spectroscopy (EDX) and XRD. Quantitative chemical analyses show that the sample is a magnesium nickel-rich carbonate with a small amount of calcium, with final composition $Ni_{0.75}Mg_{0.22}Ca_{0.03}CO_3$. XRD measurements confirmed that the sample has the calcite-type structure and the aforementioned divalent cations ratio explained well the intensities of the diffraction pattern (see Figure 1).

Thermogravimetric analysis (TGA) at ambient pressure and temperatures up to 650 ºC was carried out using the thermogravimetric analyzer TGA Q500 of TA Instruments. This test was performed under nitrogen atmosphere (sample under gas flux of 60 ml/min), at a heating rate of 2 ºC/min.

HP-XRD experiments with the magnesium gaspeite sample were conducted using gas-membrane-driven diamond-anvil cells (DACs) equipped with diamonds with 400 μm-diameter culets. We preindented the rhenium gasket to 40 μm thickness, and drilled a hole 100 μm in diameter which served as the pressure chamber. Rhenium does not react with CO_2 or carbonates below 1000 K [23-25]. HP-XRD experiments at room-temperature were carried out using He as pressure transmitting medium up to 23.3 GPa. High-purity He gas was loaded in the DAC by means of a Sanchez Technologies gas loading apparatus, and provides a fluid environment up to 11.5 GPa at room temperature [26] and a quasi-hydrostatic medium up to 25 GPa [27]. The shift of the R1 ruby fluorescence peak was used as a pressure gauge, with pressure accuracies of 0.1 GPa in the studied pressure range [28].

For the HP studies at HT, the DAC was contained within a custom-built vacuum vessel and heated using Watlow 240V coiled heaters wrapped around the outside of the DAC [29]. The maximum temperature of the experimental setup is approximately 900 K. This limitation is due to (i) the maximum voltage that one can operate these heaters, and (ii) radiative losses and coupling inefficiencies. The temperature was measured using a K-type thermocouple attached to one of the diamond anvils, close to the gasket. The uncertainty of the temperature measurements is smaller than 4 K [30-31]. KCl

powder was included in the sample chamber to act as both pressure transmitting medium and pressure marker by its thermal equation of state [32].

The magnesian gaspeite sample was characterized by *in situ* angle-dispersive powder XRD at MSPD beamline at the Spanish ALBA synchrotron using an X-ray wavelength of 0.4246 Å.[33] This beamline provides an X-ray beam focused down to ~20x20 μm^2, and the diffracted signal was collected with a Rayonix CCD detector. Integration to conventional 2θ-intensity data was carried out with the Dioptas software [34]. The indexing and refinement of the powder patterns were performed using the Chekcell [35], Unitcell [36], Powdercell [37] and Fullprof [38] program packages.

Raman spectroscopy is a versatile tool for studying the properties of carbonate minerals [39]. The HP Raman analysis was carried out up to 19 GPa with a Boehler-ALMAX type DAC equipped with two 350 μm-diameter culet diamonds. In this case we employed a stainless-steel gasket preindented to 40 μm and drilled with a hole of 150 μm. A mixture of 4:1 of methanol-ethanol served as the pressure transmitting medium and a ruby chip was used for pressure calibration [28]. $Ni_{0.75}Mg_{0.22}Ca_{0.03}CO_3$ shows an intense green color which results in an intense fluorescence background when excited with wavelengths in the visible. Additionally, the Raman active modes of $NiCO_3$ are particularly weak in comparison to those of other calcites [40]. Considering that the intensity of the Raman modes is expected to decrease under compression, minimizing the background generated under excitation is key to follow the maximum number of Raman active modes in $Ni_{0.75}Mg_{0.22}Ca_{0.03}CO_3$. For this reason, we performed the Raman spectroscopy experiments with a 785 nm diode laser. The setup consisted of a BWTEK Raman device, composed of a BWTEK BRM-OEM-785 diode laser (785 nm), a BWTEK BAC100-785E Raman head, and a BWTEK Prime T BTC661E-785CUST spectrometer with a Hamamatsu CCD (S10141-1107S, 2048 pixels) detector. The equipment covers a spectral range in Raman shift of 80–3600 cm^{-1}, with a spectral resolution of 4 cm^{-1} measured as FWHM. Spectra were acquired using commercial software provided by BWTEK. The maximum laser power was 10 mW on the sample surface and under these conditions, no thermal degradation of the materials was observed, which is normally evidenced by a drastic increase of the Raman spectrum background. The integration time

was 60 s and 2 accumulations were performed for each analysis. The Raman head was coupled to a microscope equipped with a CCD camera and a 20x microscope objective that allows us to choose the focus point of the excitation laser on the sample and a backscattering geometry was adopted to detect the optical signal.

Computational details

Calculations for ideal gaspeite ($NiCO_3$) and other isostructural minerals with variable Mg/Ni content were run using density-functional theory (DFT) in the plane-waves/ pseudopotentials approach with the projector augmented-wave (PAW) method [41] implemented in Quantum ESPRESSO [42]. We considered five different $Mg_xNi_{1-x}CO_3$ compositions with x=0, 0.25, 0.5, 0.75, and 1.0. The x=0 (ideal gaspeite) and x=1 (magnesite) cases were run using the primitive cell, with 10 atoms. For the intermediate compositions, we built 1x1x2 supercells based on the rhombohedral primitive cell with Z = 2. This resulted in unit cells with a doubled c cell length of pure gaspeite containing four Ni atoms, which we then replaced by the appropriate amount of Mg to give the 25% (1 Mg and 3 Ni atoms), 50% (2 Mg and 2 Ni), and 75% (3 Mg and 1 Ni) compositions. In the particular case of the 50% composition, there are two possibilities for arranging the Ni and Mg atoms relative to each other, resulting in two different structures: the 50%a structure with Ni at (0 0 0) and (0 0 1/2) and Mg at (1/2 1/2 1/4) and (1/2 1/2 3/4) and the 50%b structure with Ni at (0 0 0) and (1/2 1/2 1/4) and Mg at (0 0 1/2) and (1/2 1/2 3/4).

Calculations in the pure minerals were run using a 4x4x4 uniform k-point grid and wavefunction and density cutoffs of 100 and 1000 Ry, respectively, which ensures a convergence of 0.1 mRy in the total energy and 0.1 kbar in the pressure. In the intermediate-composition minerals, the number of k-points in the *c* direction was halved. In all cases, the Ni atom is in a +2 oxidation state with a d^8 electron configuration and two unpaired electrons. All calculations involving Ni atoms were run with spin-polarization and a starting magnetization aiming at an antiferromagnetic state. To improve the convergence of the self-consistent procedure, Gaussian smearing was used

with a smearing energy of 0.001 Ry. The B86bPBE [43-44] functional was used combined with the exchange-hole dipole moment (XDM) dispersion correction [45-46]. The canonical XDM parameters for B86bPBE (a1 = 0.6512, a2 = 1.4633 Å) were used [47].

Given the open-shell configuration of Ni, we considered using Hubbard's U correction [48-50] for the d-levels of the Ni atom. We employed the self-consistent approach to find the U parameter from density-functional perturbation theory (DFPT) proposed by Timrov *et al* [51]. The resulting U was equal to 5.78 eV. However, subsequent testing showed that the application of the U correction degraded the agreement with the experimental equation of state and, since we are not specifically interested in the magnetic properties of these materials, we decided to forego the use of the DFT+U energy term.

Geometry relaxations were carried out at zero pressure and under an external pressure up to 53 GPa. Tight convergence criteria were used both for the self-consistent cycle (10^{-8} Ry) and for the minimization (10^{-4} Ry/bohr in the forces, 10^{-5} Ry in the energies). The resulting equilibrium volumes were used to build a 41-point uniform volume grid. At each point in the grid, a fixed-volume minimization was carried out, followed by a phonon calculation using DFPT [52]. A uniform 2x2x2 q-point grid for the pure compositions was used, which ensures a convergence in the Helmholtz vibrational free energy of less than 0.1 kcal/mol. Similarly, a 2x2x1 uniform q-point grid was used for the mixed compositions. The structures for all compositions were dynamically and mechanically stable at all calculated pressures.

The resulting static energies and phonon density of states at each volume were used to calculate the vibrational properties and the equation of state (EOS) at room temperature. This was done using the quasi-harmonic approximation (QHA) implemented in the gibbs2 program [53-54].

Results & Discussion

Room pressure, room temperature experiments

Our magnesian gaspeite sample was characterized under ambient conditions using XRD. The positions of the diffraction peaks are perfectly explained by

the space group $R\bar{3}c$ (No. 167) with lattice parameters: a=4.6098(3) Å and c=14.7891(8) Å, and a unit cell volume V=272.17(6) Å^3. The diffraction intensities agree well with those corresponding to a calcite-type structure where the atoms of Ni and Mg are in special positions 6b and have the partial occupancy suggested by the EDX measurements, the C atoms occupy 6a Wyckoff positions and the O atoms, in positions 18e, have an atomic coordinate x_O = 0.280(2). Figure 1 shows the goodness of the Rietveld refinement. This result confirms that the stoichiometry of our sample is $Ni_{0.75}Mg_{0.22}Ca_{0.03}CO_3$. Our static theoretical calculations on pure Ni gaspeite yield similar lattice parameters (a=4.63092 Å and c=14.77204 Å, and a unit cell volume V=274.351 Å^3), leading to a volume overestimation of less than 1.0%. The static calculations considering a stoichiometry $Ni_{0.75}Mg_{0.25}CO_3$, gives a volumen per formula unit of 46.14 Å^3 (distorted non-rhombohedral symmetry), which is 0.9 % larger than the pure Ni carbonate. The relaxed position for the O atom x_O = 0.27936 in pure gaspeite is in excellent agreement with the experimental results. The calculated lattice parameters at room temperature (293 K) compared worse with the experimental data, giving slightly larger values: a=4.64499 Å and c=14.8889 Å, and a unit cell volume V=278.205 Å^3.

Although the calcite-type structure is well known [55-56], we describe it briefly to serve as a basis for the structural analysis below. The structure can be described as formed by [(Ni,Mg)O_6] octahedra and triangular planar [CO_3] carbonate groups. The atomic arrangement, depicted in Figure 2a, consists of alternating planes of carbonate groups and Ni/Mg atoms, in which each carbonate group is rotated by 60º with respect to the adjacent carbonate layers [56]. Its hexagonal lattice can also be defined by a primitive rhombohedral unit cell with a lattice parameter a'=5.5994(4) Å and an angle α=48.5817(2)º and holds 10 atoms. The atomic contents also adopt a highly distorted NaCl-like structure of Ni/Mg atoms and [CO_3] groups, in which the diagonal of the distorted B1 cubic lattice has been strongly compressed (see Figure 2b). As we will see later, this analysis in terms of the (Ni,Mg)C sublattice (that is, second-neighbour contacts) will be useful to discuss the high-pressure structural behaviour of $Ni_{0.75}Mg_{0.22}Ca_{0.03}CO_3$.

High-temperature experiments at room pressure.

The thermal stability and decomposition of our magnesian gaspeite has been studied by means of a TGA. We performed these experiments on our sample at room pressure in order to gain further insight into the gaspeite's behavior and to have it serve as a reference for high-pressure high-temperature data. The sample decomposes by releasing CO_2 in two stages (see Figure 3) centered at 441º and 550º C. The first of the mass losses begins to occur at 320º and would correspond to the decomposition of the carbonate groups only associated with the Ni and Mg atoms. This breakdown is soon followed, at 500º C, by the loss of the CO_2 molecules associated with the decomposition of a small amount of $CaCO_3$ calcite. These decomposition temperatures are in excellent agreement with those found in $Mg_3Ca(CO_3)_4$ huntite mineral in under similar experimental conditions [17]. The cumulative mass losses are 38.1% and 40.2%, respectively, which suggest that the stoichiometry of the compound is $(Ni,Mg)_{0.95}Ca_{0.05}CO_3$, in relative good agreement with EDX results.

The observed decomposition temperature of gaspeite significantly differs from that previously reported by Isaacs [11], who conducted differential thermal analyses (DTA) experiments on synthetic pure $NiCO_3$ samples and observed that decomposition began at ~280º C with the dissociation peak at 330º C. This previous study was performed at a heating rate of 4º C/min, but no reference to the gaseous medium used was given. The lower dissociation temperature could be explained if we assume that the experiments were carried out in air, since Seguin [57] observed that, at these temperatures, the rate of dissociation of gaspeite is faster in air than in nitrogen. However, our results differ even more from those reported for other magnesian gaspeite samples. Thus, Kohls and Rodda [18] stated that a $Ni_{0.49}Mg_{0.43}Fe_{0.08}CO_3$ sample heated at a rate varied from 6º to 15º C/min began to decompose slowly at 520º C, reaching the peak at 690º C. These higher decomposition temperatures could be attributed to the fact that, at a high heating rate, heat dissipates much more easily and hence decomposition starts at a comparatively higher temperature [17].

High-pressure experiments at room temperature.

Powder x-ray diffraction measurements

Synchrotron XRD measurements evidence that the rhombohedral calcite-type phase of magnesian gaspeite is stable up to 23.3 GPa, the maximum pressure reached in this study. Figure 4 shows the raw cake diffraction image and the Rietveld refinement of the XRD pattern at 1.0 GPa, to illustrate the quality of our data. Under compression, all the diffraction peaks shift to higher angles as expected for a decrease of interplanar distances, but no additional Bragg peaks are observed (see Figure 5). The intensities of the powder diffraction peaks are perfectly explained by the calculated atomic positions (x fractional coordinate of the O atom), which do not change significantly upon compression (see Table S1, in supporting information).

The experimental HP lattice parameters and the *ab initio* theoretical structural data at 0 K are collected in Tables 1 and S1, respectively. Figure 6 shows the experimental (theoretical) pressure dependence of the unit-cell volume of $Ni_{0.75}Mg_{0.22}Ca_{0.03}CO_3$ ($NiCO_3$) up to 23.3 GPa. Rather good agreement is found between experimental and calculated results. Note that the unit-cell volume decreases smoothly with pressure due to the quasi-hydrostaticity of the He used as pressure transmitting medium in the considered pressure range. The evolution of the reduced pressure ($H = P/(3 \cdot f_E \cdot (1+2 \cdot f_E)^{5/2})$) as a function of the Eulerian strain ($f_E = (1/2) \cdot ((V_0/V)^{2/3}-1)$) shows no abrupt compressibility changes even when He freezes (at 11.5 GPa). A fit of all our experimental P–V data with a 3rd-order Birch–Murnaghan EOS:

$$P(V) = \frac{3 \cdot B_0}{2} \cdot \left[\left(\frac{V_0}{V}\right)^{\frac{7}{3}} - \left(\frac{V_0}{V}\right)^{\frac{5}{3}} \right] \cdot \left\{ 1 + \frac{3}{4} \cdot (B'_0 - 4) \cdot \left[\left(\frac{V_0}{V}\right)^{\frac{2}{3}} - 1 \right] \right\}$$

yields a zero-pressure unit-cell volume V_0 = 273.79(15) Å, a bulk modulus B_0 = 105(2) GPa and a bulk modulus pressure derivative B'_0 = 7.4(3). Note that the zero-pressure volume estimated from the EOS is approximately 0.59% larger than that obtained by the room conditions Rietveld refinement. Such discrepancy is likely due to the different uncertainties associated to a single measurement and the EOS fit.

We carried out theoretical calculations for ideal gaspeite ($NiCO_3$), ideal magnesite ($MgCO_3$) and three other isostructural minerals with intermediate $Ni_xMg_{1-x}CO_3$ compositions (Ni content, x = 0.75, 0.5 and 0.25) as stated

previously. Table 2 collects the characteristic parameters of the static and room-temperature 3rd-order Birch-Murnaghan EOS that describe the compressibility of these compounds. Our results show that magnesite is significantly more compressible than ideal gaspeite, in good agreement with previous literature data [12]. The bulk moduli of the intermediate members of the $Ni_xMg_{1-x}CO_3$ system are approximately the weighted mean of the two end-member bulk moduli: $B_0(Ni_xMg_{1-x}CO_3) = x \cdot B_0(NiCO_3) + (1 - x) \cdot B_0(MgCO_3)$. The theoretical unit cell volume of magnesite at room pressure is 4.0% larger than that of gaspeite, which compares well with the 3.5% difference found experimentally [12]. This a direct consequence of the volume difference between the $[MgO_6]$ and $[NiO_6]$ octahedral units at ambient conditions. Note that in the supercells used to describe the intermediate Ni/Mg compositions, a symmetry reduction occurs due to the fact that, at ambient conditions, the $[NiO_6]$ octahedra tend to have volumes ~2% smaller than those of $[MgO_6]$ octahedra. Upon compression, this difference progressively reduces and, above 27 GPa, the $[NiO_6]$ octahedra become larger in all the calculated compositions (just where the magnesite P-V curve crosses that of gaspeite, see Figure 6).

Our theoretical data confirms the experimental observation that $NiCO_3$ gaspeite is the most incompressible of all the divalent metal carbonates [12]. Even a magnesian gaspeite with composition $Ni_{0.75}Mg_{0.22}Ca_{0.03}CO_3$ has a larger bulk modulus than $CaCO_3$ calcite (B_0=67(2) GPa) [12], $CdCO_3$ otavite (B_0=97(1) GPa) [12], $MgCO_3$ magnesite (B_0=107(1) GPa, and B_0=97.1(5) and B'_0=5.44(7)) [12, 58], $MnCO_3$ rhodochrosite (B_0=108(1) GPa) [12], $FeCO_3$ siderite (B_0=117(1) GPa) [12], and a comparable value to that of $ZnCO_3$ smithsonite (B_0=124(1) GPa) [12] and $CoCO_3$ spherocabaltite (B_0=125(1) GPa) [12].

An analysis in terms of linear axial compressibilities (β) of our magnesian gaspeite reveals that this mineral is highly anisotropic, the c axis being much more compressible than the a axis (see Figure 7). Although the lattice parameters decrease smoothly with pressure, we only estimate the linear axial compressibilities before the solidification of He used as pressure medium: $\beta a = 1.62(3) \cdot 10^{-3}$ GPa^{-1} and $\beta c = 3.84(6) \cdot 10^{-3}$ GPa^{-1}. As can be seen in Figure 8, the relative axial compression of the unit-cell axes predicted by our calculations for pure $NiCO_3$ show an excellent agreement with our

experimental data. The anisotropy of compressibility is similar to those reported for Co and Zn carbonates [12], with a decrease of the c/a axes ratio with increasing pressure according to the expression c/a = 3.203(1) – 0.0068(2)·P (in the range 0 – 11.5 GPa). This response to external pressure arises from the fact that the relatively incompressible [CO_3] carbonate units are arranged parallel to the ab plane, whereas the compressibility of the c axis is directly attributable to the [(Ni,Mg,Ca)O_6] octahedral compression.

The structural changes observed in magnesian gaspeite under compression, like other oxides, can also be rationalized in terms of the second coordination sphere of the metallic atoms [59-62]. The decrease of the hexagonal distortion of the lattice, which is described by the approach of the $t = 2a\sqrt{2}/c$ parameter to 1 [63], causes the cation (Ni,Mg,Ca)C substructure, described in the Introduction section as a highly distorted NaCl-type network at room pressure, to progressively evolve towards a CsCl-type conformation (see Figure 9). The [CO_3]-centered [Ni_8] pseudo cubes become more regular with increasing pressure, adopting a ∠Ni-Ni-Ni angle of 80.8º at 23.3 GPa, which means that the second coordination sphere of the carbonate optimizes its packing progressively. This alternative structural analysis provides much more information than just the smooth compression of [(Ni,Mg,Ca)O_6] units obtained when analyzing the first-coordination sphere.

Raman spectroscopy measurements

In carbonate minerals with the calcite structure (D^6_{3d}) there is one A_{1g} mode and four doubly degenerate E_g modes at the Γ point of the Brillouin zone.

$$\Gamma_{Raman} = A_{1g} + 4E_g$$

In particular, two of the four E_g modes and the A_{1g} mode can be assigned as internal phonons of the CO_3 polyhedra, while the remaining two E_g modes are a libration E_g(L) and translation E_g(T) mode of the CO_3 polyhedra in the primitive unit cell, respectively.

The Raman spectrum of $Ni_{0.75}Mg_{0.22}Ca_{0.03}CO_3$ at different pressures is shown in Fig. 10. We can only observe the E_g(T), the E_g(L), and the intense CO_3 breathing A_{1g} modes. Their frequencies, 229, 338, and 1086 cm^{-1} agree well with the previously reported values [64], considering that we have a ~20 wt% of Mg in our sample, which is expected to lower the frequency of our modes

relative to the values reported by Rutt and Nicola [64] for synthetic $NiCO_3$. Under compression the three observed modes fade, the weakest E_g(T) mode vanishes at 4 GPa and the E_g(L) can barely be followed above 10 GPa. The intense A_{1g} mode is easily seen up to 19 GPa, the maximum pressure reached in this experiment. The pressure-dependence of the frequency of the three modes is shown in Figure 11. Under compression, most of the contraction is accommodated by the larger NiO_6 polyhedra with the CO_3 polyhedra being less compressible and the alternating Ni-C-Ni planes {111} getting closer. Considering that the eigenvector of the E_g(L) mode moves the O atoms along the [111] direction, this results into a faster frequency increase of the translational E_g(L) mode (4.2 cm^{-1}/GPa) with respect to the other two modes (3.2 cm^{-1}/GPa for E_g(T) and 3.5 cm^{-1}/GPa for the A_{1g}).

The sensitivity of the E_g(T) and the A_{1g} modes to the presence of a different metallic ion in carbonates has been proposed as a way to estimate the composition of natural carbonate rocks. According to Dufresne, Rufledt, and Marshall [40] the frequency of the intense A_{1g} mode decreases at -27 cm^{-1}/Å with the A-O bond distance, and the frequency of the E_g(T) mode decreases at -2 cm^{-1}/pm with the ionic radius. In the case of our magnesian gaspeite, with the ionic radius of Ni and Mg being 69 and 72 pm, respectively, the dependence law obtained by Dufresne, Rufledt, and Marshall [40] with a resolution of ~5 pm does not allow us to obtain information on the composition of our natural sample. Even though our Raman measurements (4 cm^{-1} of resolution) do not allow us to observe differences in the frequencies between $NiCO_3$ and our natural $Ni_{0.75}Mg_{0.22}Ca_{0.03}CO_3$ sample, we have explored the dependence of the A_{1g} mode with both the C-O and the (Ni,Mg)-O bond distances. According to our *ab initio* calculations, under pressure the *x* coordinate of O only changes from 0.2794 (room conditions) to 0.2838 (23 GPa). Thus, assuming that it remains nearly constant we have estimated the (Ni,Mg)-O and the C-O distances with pressure and obtained the change in the mode frequency with both distances. The result shows that the A_{1g} breathing mode varies at -2300 cm^{-1}/Å with the C-O bond distance and -700 cm^{-1}/Å with the (Ni,Mg)-O bond distance. The result in $FeCO_3$, obtained with data from Ref. [65] is the same as with $Ni_{0.75}Mg_{0.22}Ca_{0.03}CO_3$. So far, it has been considered that using the frequency dependence with the C-O distance does

not provide enough sensitivity to identify carbonates with different compositions [41]. For this reason, the frequency dependence with the *A*-O distance or the ionic radius of *A* has been employed. We have demonstrated that the A_{1g} mode is very sensitive (-2300 cm^{-1}/Å) to the C-O bond in a single carbonate. Considering that the frequency of the A_{1g} mode changes at -100 cm^{-1}/Å according to the data published in Ref. [40], the calibration of the most intense A_{1g} mode with the C-O bond appears to be a precise way to distinguish between different carbonates.

High-pressure high-temperature experiments

Magnesian gaspeite $Ni_{0.75}Mg_{0.22}Ca_{0.03}CO_3$ was also simultaneously compressed and heated. In this experiment we first increased pressure to 5.5 GPa and subsequently heated up to 840 K. Our results show that, at this pressure, the magnesian gaspeite is stable to the maximum temperature reached in this study. This observation is consistent with the decomposition temperatures at different pressures of pure nickel carbonate reported by Isaacs [11]. The phase diagram proposed by this researcher suggests that, in the 0 – 2.5 GPa pressure range, the temperature at which pure gaspeite decomposes follows the expression: T(K) = 593 + 160(20) · P(GPa). Moreover, the partial substitution of Ni atoms by Mg is also expected to increase the thermal stability with pressure of our magnesian gaspeite, since magnesite is supposed to be the stable carbonate phase at the pressure and temperature conditions of the Earth's mantle [13].

We have studied the thermal expansion of $NiCO_3$ at room pressure and 5.5 GPa by means of our *ab initio* calculations. Figure 12 reports the lattice parameters and volume with increasing temperature for gaspeite. From our theoretical calculations the mean linear thermal expansion coefficients for the lattice parameters and volume have been obtained with the equation:

$$\alpha_X = \frac{1}{X_{290}} \cdot \frac{X_T - X_{290}}{T - 290}$$

where *X* stands for the parameter to be studied (i.e. *a* axis, *c* axis or unitcell volume). The reference temperature is 290 K and $(X_T - X_{290})/(T - 290)$ is the slope of the straight line obtained from a linear fit of *X* vs temperature data.

This linear regression analysis has been carried out in the temperature range 290-450 K (290-500 K) at room pressure (5.5 GPa) where the dependence of lattice parameters and volume with temperature is linear. The obtained values for the theoretical thermal expansion coefficients for the lattice parameters are α_a = 8.2·10^{-6} K^{-1} and α_c = 21·10^{-6} K^{-1} at room pressure and α_a = 5.8·10^{-6} K^{-1} and α_c = 15·10^{-6} K^{-1} at 5.5 GPa. Axial thermal expansion coefficients are smaller at 5.5 GPa than at room pressure. The axial thermal expansion coefficients ratio is $\frac{\alpha_c}{\alpha_a}$ = 2.6 (2.5) at room pressure (5.5 GPa) indicating that the expansion along *c* axis is about three times greater than that along *a* axis. This anisotropy in the lattice thermal expansion is similar to that obtained experimentally at room pressure for other calcite-type carbonates such us $MgCO_3$ and $MnCO_3$ [66-67], with comparable axial thermal expansion coefficients. On the other hand, the obtained value for the theoretical volumetric thermal expansion coefficient, from a fit of volume vs temperature data, is α_{vol} =38·10^{-6} K^{-1} (26·10^{-6} K^{-1}) at room pressure (5.5 GPa). This value of α_{vol} at room pressure (5.5 GPa) can also be obtained with $\alpha_{vol} = 2 \cdot \alpha_a + \alpha_c$ = 38·10^{-6} K^{-1} (26·10^{-6} K^{-1}).

We experimentally determined the Birch−Murnaghan EOS of our magnesian gaspeite at ~846 K with 18 P-V data points in the range of 5.5−21 GPa. The lattice parameters and unit cell volumes of this calcite-type structure at this temperature and different pressures are collected in Table 3. If B_0' is left to vary freely, we obtain as characteristic parameters at that temperature a zero-pressure volume of 281.77(14) Å^3, a bulk modulus of 81.5(7) GPa and a bulk modulus first-pressure derivative of 8.4(3). The EOS fit was also carried out fixing the B_0' to 4.64 in order to better compare to the compressional results at ambient temperature, yielding the following values: $V_{0,846K}$ =278.4(4) Å^3 and $B_{0,840K}$=114.6(1).

Conclusions

The calcite-type structure is very common among $M^{II}CO_3$ carbonates and it can naturally accommodate several divalent cation species with different

radii; *i.e*. Mg^{2+}, Ca^{2+}, Fe^{2+}, Mn^{2+}, etc.... However, the effect of cation substitutions on the stability of this type of minerals is not yet fully understood. Pure nickel carbonate $NiCO_3$ seems not to occur as a natural calcite-type mineral but has been synthesized by hydrothermal conditions in the laboratory. In nature, the Ni^{2+} cations of an ideal gaspeite are partially substituted by other divalent cations, mainly Mg^{2+}, and stoichiometries varying from 50% to 90% Ni content have been found [20, 68]. In this work, we have studied the structural behavior of the naturally-occurring mineral of composition $Ni_{0.75}Mg_{0.22}Ca_{0.03}CO_3$ with increasing pressures and temperatures. At ambient pressure, magnesian gaspeite starts decomposing into the corresponding binary oxides and carbon dioxide at ~620 K, a relatively low temperature. The stability of this calcite-type compound to decomposition improves significantly upon compression. Pressure does not produce any phase transition up to 23.3 GPa at ambient temperature or up to 21 GPa at ~ 846 K. We have accurately determined the equations of state at ambient temperature using He as a pressure medium and at ~ 846 K, where thermal annealing reduces the non-hydrostatic stresses of the solid KCl pressure medium. To complement our experimental data, we performed *ab initio* total-energy calculations of 5 different compositions along in the $NiCO_3$-$MgCO_3$ family. Our results show that the bulk moduli of the intermediate members of the $Ni_xMg_{1-x}CO_3$ system are approximately the weighted mean of the two end-members $NiCO_3$ and $MgCO_3$ bulk moduli. The fact that carbonate units are highly incompressible entails that the compression of the structure is dependent on the reduction of the $[(Ni/Mg)O_6]$ octahedral units. Finally, our data have been compared to previous results of other calcite-type carbonates. The experiment on gaspeite at 5.5 GPa under increasing temperature up to 840 K has shown that this mineral undergoes positive thermal expansion and it is stable at these conditions. Our *ab initio* simulations on $NiCO_3$ at zero pressure and 5.5 GPa under high temperature report linear axial thermal expansion coefficients of α_a = $8.2 \cdot 10^{-6}$ K^{-1} and α_c = $21 \cdot 10^{-6}$ K^{-1} at zero pressure in the 290-450 K temperature range, and α_a = $5.8 \cdot 10^{-6}$ K^{-1} and α_c = $15 \cdot 10^{-6}$ K^{-1} at 5.5 GPa in the 290-500 K temperature range. The $\frac{\alpha_c}{\alpha_a}$ = 2.6 (2.5) ratio at zero pressure (at 5.5 GPa) highlights the

high anisotropy in axial thermal expansion which is comparable to the anisotropy found in axial compressibility.

This study reports valuable crystallographic data of the high-pressure high-temperature behavior of magnesian gaspeite which contribute to the understanding of the carbonate crystal chemistry.

Supporting Information

Table collecting the calculated unitcell volumes, lattice parameters and x atomic coordinate of the O atom for pure $NiCO_3$ at different pressures and 0 K.

Acknowledgements

Authors thank the financial support from the Spanish Ministerio de Ciencia, Innovación y Universidades (MICINN) under projects MALTA Consolider Ingenio 2010 network (MAT2015-71070-REDC) and PGC2018-097520-A-I00, and from the Generalitat Valenciana under project PROMETEO/2018/123. D.S.-P. and A.O.R. acknowledge the financial support of the Spanish MINECO for the RyC-2014-15643 and RyC-2016-20301 Ramon y Cajal Grants, respectively. C.P and O.G acknowledge the financial support from the Spanish Ministerio de Economia y Competitividad (MINECO projects FIS2017-83295-P and MAT2016-75586-C4-1-P/2-P, respectively). We thank David Vie for carrying out the GTA measurements. Authors also thank Dr. Nicolescu and the Mineralogy and Meteroritic Department of the Yale Peabody Museum of Natural History for providing the mineral samples, and ALBA-CELLS synchrotron for providing beamtime under experiment 2018082948. A.O.R. thanks the MALTA Consolider supercomputing centre and Compute Canada for computational resources.

References

1. Dasgupta, R., Ingassing, storage, and outgassing of terrestrial carbon through geologic time. *Rev. Mineral. Geochemistry* **2013,** *75*, 183–229
2. Connolly, J. A. D., Computation of phase equilibria by linear programming: A tool for geodynamic modeling and its application to subduction zone decarbonation. *Earth Planet. Sci. Lett.* **2005,** *236*, 524–541.
3. Rohrbach, A.; Schmidt, M. W., Redox freezing and melting in the Earth's deep mantle resulting from carbon-iron redox coupling. *Nature* **2011,** *472*, 209–214.
4. Stagno, V.; Ojwang, D. O.; McCammon, C. A.; Frost, D. J., The oxidation state of the mantle and the extraction of carbon from Earth's interior. *Nature* **2013,** *493*, 84-88.
5. Litasov, K. D.; Shatskiy, A., Carbon-Bearing Magmas in the Earth's Deep Interior In *Magmas Under Pressure*, Elsevier: 2018; pp 43-82.
6. Brenker, F. E.; Vollmer, C.; Vinczec, L.; Vekemans, B.; Szymanskia, A.; Janssens, K.; Szalokie, I.; Nasdala, L.; Joswig, W.; Kaminsky, F., Carbonates from the lower part of transition zone or even the lower mantle. *Earth Planet. Sci. Lett.* **2007,** *260*, 1-9.
7. Stachel, T.; Harris, J. W.; Brey, G. P.; Joswig, W., Kankan diamonds (Guinea) II: Lower mantle inclusion parageneses. *Contrib. Mineral. Petrol.* **2000,** *140*, 16-27.
8. Boulard, E.; Pan, D.; Galli, G.; Liu, Z.; Mao, W. L., Novel carbon bonding at high pressure. *Nature Communications* **2015,** *6*, 6311.
9. Santamaria-Perez, D.; Ruiz-Fuertes, J.; Marqueño, T.; Pellicer-Porres, J.; Chulia-Jordan, R.; MacLeod, S.; Popescu, C., Structural behavior of natural silicate–carbonate spurrite mineral, Ca5(SiO4)2(CO3), under high-pressure, high-temperature conditions. *Inorg. Chem.* **2018,** *57*, 98-105.
10. Santamaria-Perez, D.; Ruiz-Fuertes, J.; Peña-Alvarez, M.; Chulia-Jordan, R.; Marqueño, T.; Zimmer, D.; Gutierrez-Cano, V.; MacLeod, S.; Gregoryanz, E.; Popescu, C.; Rodriguez-Hernandez, P.; Muñoz, A., Post-tilleyite, a dense calcium silicate-carbonate phase. *Scientific Reports* **2019,** *9*, 7898.
11. Isaacs, T., The mineralogy and chemistry of the nickel carbonates. *Mineral. Mag. J. Mineral. Soc.* **1963,** *33*, 663–678
12. Zhang, J.; Reeder, R. J., Comparative compressibilities of calcite-structure carbonates: Deviations from empirical relations. *Am. Mineral.* **1999,** *84*, 861–870
13. Isshiki, M.; Irifune, T.; Hirose, K.; Ono, K.; Ohishi, Y.; Watanuki, T.; Nishibori, E.; Takata, M.; Sakata, M., Stability of magnesite and its high-pressure form in the lowermost mantle. *Nature* **2004,** *427*, 60–63.
14. Suito, K.; Namba, J.; Horikawa, T.; Taniguchi, Y.; Sakurai, N.; Kobayashi, M.; Onodera, A.; Shimomura, O.; Kikegawa, T., Phase relations of CaCO3 at high pressure and high temperature. *Am. Mineral.* **2001,** *86*, 997–1002
15. Merlini, M.; Hanfland, M.; Crichton, W. A., CaCO 3-III and CaCO 3-VI, high-pressure polymorphs of calcite: Possible host structures for carbon in the Earth's mantle. *Earth Planet. Sci. Lett.* **2012,** *333–334*, 265–271
16. Merlini, M.; Crichton, W. A.; Hanfland, M.; Gemmi, M.; Müller, H.; Kupenko, I.; Dubrovinsky, L., Structures of dolomite at ultrahigh pressure and their influence on the deep carbon cycle. *PNAS* **2012,** *109*, 13509-13514.

17. Santamaria-Perez, D.; Otero-de-la-Roza, A.; Ruiz-Fuertes, J.; Chulia-Jordan, R.; Marqueño, T.; MacLeod, S.; Popescu, C., Pressure and temperature effects on low-density Mg3Ca(CO3)4 huntite carbonate. *J. Phys. Chem. C* **2020,** *124*, 1077-1087.
18. Kohls, D. W.; Rodda, J. L., Gaspeite, (Ni, Mg, Fe)(CO3), a new carbonate from the gaspé Peninsula, Quebec. *Am. Mineral.* **1966,** *51*, 677–684
19. Mariano, A. N.; Pojasek, W. J.; Bender, W. L., Nickel-carbonate from northeast Transvaal. *Can. Mineral.* **1969,** *10*, 139–140.
20. Nickel, E. H., An occurrence of gaspéite and pecoraite in the Nullagine region of Western Australia. *Mineral. Mag.* **1973,** *39*, 113–115.
21. Gaines, A. M.; Goldsmith, J. R., Crystal chemistry and stability relations in the system MgCO3-NiCO3. *Zeitschrift für Krist.* **1971,** *133*, 432–444
22. Langlès, R. S. L., Préparation et structure du carbonate neutre de nickel anhydre cristallisé. *Ann. Chim.* **1952,** *7*, 568–583.
23. Santamaria-Perez, D.; McGuire, C.; Makhluf, A.; Kavner, A.; Chulia-Jordan, R.; Jorda, J. L.; Rey, F.; Pellicer-Porres, J.; Martinez-Garcia, D.; Rodriguez-Hernandez, P.; Muñoz, A., Strongly-driven Re + CO2 redox reaction at high-pressure and high-temperature. *Nature Commun.* **2016,** *7*, 13647.
24. Santamaria-Perez, D.; McGuire, C.; Makhluf, A.; Kavner, A.; Chulia-Jordan, R.; Pellicer-Porres, J.; Martinez-Garcia, D.; Doran, A.; Kunz, M.; Rodriguez-Hernandez, P.; Muñoz, A., Exploring the chemical reactivity between carbon dioxide and three transition metals (Au, Pt, Re) at high-pressure, high-temperature conditions. *Inorg. Chem.* **2016,** *55*, 10793-10799.
25. Chulia-Jordan, R.; Santamaria-Perez, D.; Marqueño, T.; Ruiz-Fuertes, J.; Daisenberger, D., Oxidation of high yield strength metals tungsten and rhenium in high-pressure high-temperature experiments of carbon dioxide and carbonates. *Crystals* **2019,** *9*, 676.
26. Santamaría-Pérez, D.; Mukherjee, G. D.; Schwager, B.; Boehler, R., High-pressure melting curve of helium and neon: Deviations from corresponding states theory. *Phys. Rev. B - Condens. Matter Mater. Phys.* **2010,** *81*, 214101.
27. Klotz, S.; Chervin, J. C.; Munsch, P.; Le Marchand, G., Hydrostatic limits of 11 pressure transmitting media. *J. Phys. D. Appl. Phys.* **2009,** *42*, 075413.
28. Mao, H. K.; Xu, J.; Bell, P. M., Calibration of the ruby pressure gauge to 800 kbar under quasi-hydrostatic conditions. *J. Geophys. Res.* **1986,** *91*, 4673.
29. Ruiz-Fuertes, J.; Martínez-García, D.; Marqueño, T.; Errandonea, D.; MacLeod, S. G.; Bernert, T.; Haussühl, E.; Santamaría-Pérez, D.; Ibáñez, J.; Mallavarapu, A.; Achary, S. N.; Popescu, C.; Bettinelli, M., High-Pressure High-Temperature Stability and Thermal Equation of State of Zircon-Type Erbium Vanadate. *Inorg. Chem.* **2018,** *57*, 14005–14012.
30. Santamaría-Pérez, D.; Marqueño, T.; MacLeod, S.; Ruiz-Fuertes, J.; Daisenberger, D.; Chuliá-Jordan, R.; Errandonea, D.; Jordá, J. L.; Rey, F.; McGuire, C.; Mahkluf, A.; Kavner, A.; Popescu, C., Structural Evolution of CO2-Filled Pure Silica LTA Zeolite under High-Pressure High-Temperature Conditions. *Chem. Mater.* **2017,** *29*, 4502–4510.
31. Marqueño, T.; Santamaria-Perez, D.; Ruiz-Fuertes, J.; Chuliá-Jordán, R.; Jordá, J. L.; Rey, F.; McGuire, C.; Kavner, A.; MacLeod, S.; Daisenberger, D.; Popescu, C.; Rodriguez-Hernandez, P.; Muñoz, A., An Ultrahigh CO2-Loaded Silicalite-1 Zeolite: Structural Stability and Physical Properties at High Pressures and Temperatures. *Inorg. Chem.* **2018,** *57*, 6447–6455.
32. Walker, D.; Cranswick, L. M. D.; Verma, P. K.; Clark, S. M.; Buhre, S., Thermal equations of state for B1 and B2 KCl. *American Mineralogist* **2002,** *87*, 805-812
33. Fauth, F.; Peral, I.; Popescu, C.; Knapp, M., The new Material Science Powder Diffraction beamline at ALBA Synchrotron. *Powder Diffr.* **2013,** *28*, 360–370.
34. Prescher, C.; Prakapenka, V. B., DIOPTAS: A program for reduction of two-dimensional X-ray diffraction data and data exploration. *High Press. Res.* **2015,** *35*, 223–230.
35. Laugier, J.; Bochu, B., Checkcell, LMGP-Suite Suite of Programs for the interpretation of X-ray Experiments. http://www.inpg.fr/LMGP. **2004**.

36. Holland, T. J. B.; Redfern, S. A. T., Unit cell refinement from powder diffraction data: the use of regression diagnostics. *Mineral. Mag.* **1997,** *61*, 65-77.
37. Kraus, W.; Nolze, G., POWDER CELL – a program for the representation and manipulation of crystal structures and calculation of the resulting X-ray powder patterns. *J. Appl. Crystallogr.* **1996,** *29*, 301–303.
38. Rodríguez-Carvajal, J., Recent advances in magnetic structure determination by neutron powder diffraction. *Phys. B Condens. Matter* **1993,** *192*, 55-69.
39. Bonales, L. J.; Muñoz-Iglesias, V.; Santamaria-Perez, D.; Caceres, M.; Fernandez-Remolar, D.; Prieto-Ballesteros, O., Quantitative Raman spectroscopy as a tool to study the kinetics and formation mechanism of carbonates. *Spectrochimica Acta A* **2013,** *116*, 26-30.
40. Dufresne, W. J. B.; Rufledt, C. J.; Marshall, C. P., Raman spectroscopy of the eight natural carbonate minerals of calcite structure. *J. Raman Spectrosc.* **2018,** *49*, 1-9.
41. Blöchl, P. E., Projector augmented-wave method. *Phys. Rev. B* **1994,** *50*, 17953–17979.
42. Giannozzi, P.; Andreussi, O.; Brumme, T.; Bunau, O.; Buongiorno Nardelli, M.; Calandra, M.; Car, C.; Cavazzoni, C.; Ceresoli, D.; Cococcioni, M.; Colonna, N.; Carnimeo, I.; Dal Corso, A.; de Gironcoli, S.; Delugas, P.; DiStasio Jr, R. A.; Ferretti, A.; Floris, A.; Fratesi, G.; Fugallo, G.; Gebauer, R.; Gerstmann, U.; Giustino, F.; Gorni, T.; Jia, J.; Kawamura, M.; Ko, H.-Y.; Kokalj, A.; Küçükbenli, E.; Lazzeri, M.; Marsili, M.; Marzari, N.; Mauri, F.; Nguyen, N. L.; Nguyen, H.-V.; Otero-de-la-Roza, A.; Paulatto, L.; Poncé, S.; Rocca, D.; Sabatini, R.; Santra, B.; Schlipf, M.; Seitsonen, A. P.; Smogunov, A.; Timrov, I.; Thonhauser, T.; Umari, P.; Vast, N.; Wu, X.; Baroni, S., Advanced capabilities for materials modelling with Quantum ESPRESSO. *J. Phys. Condens. Matter* **2017,** *29*, 465901.
43. Becke, A. D., On the large-gradient behavior of the density functional exchange energy. *J. Chem. Phys.* **1986,** *85*, 7184–7187
44. Perdew, J. P.; Burke, K.; Ernzerhof, M., Generalized gradient approximation made simple. *Phys. Rev. Lett.* **1996,** *77*, 3865–3868.
45. Becke, A. D.; Johnson, E. R., Exchange-hole dipole moment and the dispersion interaction revisited. *J. Chem. Phys.* **2007,** *127*, 154108-154114.
46. Otero-De-La-Roza, A.; Johnson, E. R., Van der Waals interactions in solids using the exchange-hole dipole moment model. *J. Chem. Phys.* **2012,** *136*, 174109.
47. Johnson, E. R., http://schooner.chem.dal.ca/wiki/XDM.
48. Anisimov, V. I.; Zaanen, J.; Andersen, O. K., Band theory and Mott insulators: Hubbard U instead of Stoner I. *Phys. Rev. B* **1991,** *44*, 943–954.
49. Anisimov, V. I.; Solovyev, I. V.; Korotin, M. A.; Czyyk, M. T.; Sawatzky, G. A., Density-functional theory and NiO photoemission spectra. *Phys. Rev. B Condens Matter* **1993,** *48*, 16929–16934.
50. Lichtenstein, A. I.; Anisimov, V. I.; Zaanen, J., Density-functional theory and strong interactions: Orbital ordering in Mott-Hubbard insulators. *Phys. Rev. B* **1995,** *52*, 5467–5471.
51. Timrov, I.; Marzari, N.; Cococcioni, M., Hubbard parameters from density-functional perturbation theory. *Phys. Rev. B* **2018,** *98*, 085127.
52. Baroni, S.; de Gironcoli, S.; Dal Corso, A.; Giannozzi, P., Phonons and related crystal properties from density-functional perturbation theory. *Rev. Mod. Phys.* **2001,** *73*, 515–562.
53. Otero-De-La-Roza, A.; Abbasi-Pérez, D.; Luaña, V., Gibbs2: A new version of the quasiharmonic model code. II. Models for solid-state thermodynamics, features and implementation. *Comput. Phys. Commun.* **2011,** *182*, 2232–2248.
54. Otero-De-La-Roza, A.; Luaña, V., Gibbs2: A new version of the quasi-harmonic model code. I. Robust treatment of the static data. *Comput. Phys. Commun.* **2011,** *182*, 1708–1720.
55. Santamaría-Perez, D.; Gomis, O.; Sans, J. A.; Ortiz, H. M.; Vegas, A.; Errandonea, D.; Ruiz-Fuertes, J.; Martinez-Garcia, D.; Garcia-Domene, B.; Pereira, A. L. J.; Manjon, F. J.; Rodríguez-Hernandez, P.; Muñoz, A.; Piccinelli, F.; Bettinelli, M.; Popescu, C., Compressibility Systematics of Calcite-Type Borates: An Experimental and Theoretical Structural Study on ABO3 (A = Al, Sc, Fe, and In). *J. Phys. Chem. C* **2014,** *118*, 4354−4361.

56. Skinner, A. J.; LaFemina, J. P.; Jansen, H. J. F., Structure and bonding of calcite: A theoretical study. *Am. Mineral.* **1994,** *79*, 205-214.
57. Seguin, M. K., The stability of gaspeite in inert atmospheres and in air. *Canadian Mineralogist* **1973,** *12*, 26-32.
58. Litasov, K. D.; Fei, Y.; Ohtani, E.; Kuribayashi, T., Thermal equation of state of magnesite to 32 GPa and 2073 K. *Physics of the Earth and Planetary Interiors* **2008,** *168*, 191-203.
59. Santamaría-Pérez, D.; Chuliá-Jordán, R., Compression of mineral barite, BaSO4: a structural study. *High Press. Res.* **2012,** *32*, 81-88.
60. Santamaria-Perez, D.; Vegas, A.; Liebau, F., The Zintl-Klemm Concept Applied to Cations in Oxides. II. The Structure of Silicates. *Struct. Bonding* **2005,** *118*, 121−177.
61. Vegas, A.; Jansen, M., Structural relationships between cations and alloys; an equivalence between oxidation and pressure. *Acta Crystallogr. B* **2002,** *58*, 38-51.
62. Vegas, A.; Mattesini, M., Towards a generalized vision of oxides: Disclosing the role of cations and anions in determining unit-cell dimensions. *Acta Crystallogr., B* **2010,** *66*, 338-344.
63. Redfern, S. A. T.; Angel, R. J., *Contrib. Mineral. Petrol.* **1999,** *134*, 102−106.
64. Rutt, H. N.; Nicola, J. H., Raman spectra of carbonates of calcite structure. *Journal of Physics C: Solid State Physics* **1974,** *7*, 4522-4528.
65. Farfan, G.; Wang, S.; Ma, h.; Caracas, R.; Mao, W. L., Bonding and structural changes in siderite at high pressure. *American Mineralogist* **2012,** *97*, 1421-1426.
66. Liang, W.; Li, L.; Li, R.; Yin, Y.; Li, Z.; Liu, X.; Shan, S.; He, Y.; Meng, Y.; Li, Z.; Li, H., Crystal structure of impurity-free rhodochrosite (MnCO3) and thermal expansion properties. *Phys. Chem. Minerals* **2020,** *47*, 9.
67. Markgraf, S. A.; Reeder, R. J., High-temperature structure refinements of calcite and magnesite. *Am. Mineral.* **1985,** *70*, 590-600.
68. Maksimovic, Z. M., *Recueil des Travaux Académie Serbe des Sciences* **1952,** *23*, 21.

749 Table 1.- Experimental lattice parameters and unit-cell volumes of the
750 rhombohedral $R\bar{3}c$ $Ni_{0.75}Mg_{0.22}Ca_{0.03}CO_3$ compound at different pressures and
751 room temperature, from LeBail refinements.

752

Pressure (GPa)	*a* axis (Å)	*c* axis (Å)	Unitcell Volume (Å^3)
1E-4	4.6069(5)	14.781(3)	271.68(1)
0.4	4.6130(7)	14.782(4)	272.41(2)
1.0	4.6093(7)	14.748(4)	271.34(2)
1.6	4.6030(7)	14.710(4)	269.92(2)
2.3	4.5976(8)	14.659(4)	268.34(2)
3.0	4.5910(8)	14.635(4)	267.14(2)
3.7	4.5853(9)	14.574(5)	265.36(2)
4.7	4.5774(8)	14.518(4)	263.44(2)
5.7	4.5708(8)	14.464(5)	261.70(2)
6.6	4.5640(9)	14.412(5)	259.99(2)
7.7	4.5573(9)	14.356(6)	258.22(2)
8.7	4.5504(9)	14.302(6)	256.47(2)
9.8	4.5430(9)	14.255(6)	254.78(2)
11.0	4.5371(10)	14.196(6)	253.08(2)
13.0	4.5233(11)	14.112(7)	250.06(3)
14.0	4.5214(11)	14.075(7)	249.18(3)
15.5	4.5146(11)	14.019(7)	247.44(3)
16.8	4.5081(12)	13.966(7)	245.81(3)
18.3	4.5011(12)	13.917(7)	244.18(3)
19.4	4.4966(13)	13.877(8)	242.98(3)
20.9	4.4909(13)	13.830(7)	241.56(3)
22.2	4.4850(14)	13.787(8)	240.17(3)
23.3	4.4799(14)	13.749(8)	238.97(3)

753

754

Table 2.- List of zero-pressure unit-cell volumes (V_0), bulk moduli (B_0) and their first-pressure derivatives (B_0') for the experimental $Ni_{0.75}Mg_{0.22}Ca_{0.03}CO_3$ magnesian gaspeite at ambient temperature and calculated $Ni_xMg_{1-x}CO_3$ stoichiometries (x=1, 0.75, 0.5, 0.25, and 0) using a 3rd-order Birch-Murnaghan EOS. Static theoretical data (0 K) are given for all the different compositions, whereas room temperature data (298 K) are given only for Ni and Mg end-members (pure gaspeite and magnesite). The experimental parameters of pure $NiCO_3$ from literature [Ref. 12] are given for the sake of comparison.

Sample	Data	T (K)	V_0 (Å^3)	B_0 (GPa)	B_0'
$NiCO_3$, gaspeite	Experimental [Ref. 12]	298	270.15(12)	131(1)	4(fixed)
$NiCO_3$, gaspeite	Calculated, B86bPBE	0	273.95	129.26	4.64
		298	277.99	122.28	4.72
$Ni_{0.75}Mg_{0.22}Ca_{0.03}CO_3$ Magnesian gaspeite	Experimental	298	273.79(15)	105(2)	7.4(3)
		298	272.6(2)	128.1(14)	4.64(fixed)
		298	272.7(2)	127.4(14)	4.72(fixed)
$Ni_{0.75}Mg_{0.25}CO_3$	Calculated, B86bPBE	0	276.81	123.06	4.60
$Ni_{0.5}Mg_{0.5}CO_3$		0	279.77	117.24	4.56
		0	279.54	117.68	4.57
$Ni_{0.25}Mg_{0.75}CO_3$		0	282.36	112.47	4.52
$MgCO_3$, magnesite		0	285.05	107.78	4.48
		298	290.14	99.89	4.67

768 Table 3.- Experimental lattice parameters and unit-cell volumes of the
769 rhombohedral $R\bar{3}c$ $Ni_{0.75}Mg_{0.22}Ca_{0.03}CO_3$ compound at different pressures and
770 a temperature of ~ 846 K, from LeBail refinements.

771

Temperature (K)	Pressure (GPa)	a axis (Å)	c axis (Å)	Unitcell Volume (Å^3)
840	5.5	4.5844(13)	14.660(9)	266.83(14)
845	5.6	4.5837(13)	14.653(9)	266.62(14)
845	6.0	4.5811(13)	14.633(9)	265.95(14)
845	6.2	4.5791(13)	14.615(9)	265.39(14)
846	7.4	4.5716(14)	14.552(9)	263.38(15)
846	8.6	4.5624(14)	14.485(9)	261.12(15)
846	11.0	4.5462(14)	14.360(9)	257.03(15)
846	12.1	4.5390(14)	14.307(9)	255.27(15)
846	12.7	4.5354(14)	14.275(9)	254.30(17)
846	13.5	4.5305(15)	14.237(9)	253.07(17)
846	14.4	4.5238(15)	14.195(9)	251.58(17)
846	15.3	4.5189(15)	14.156(9)	250.34(17)
846	16.7	4.5124(15)	14.108(9)	248.78(17)
846	17.4	4.5084(15)	14.077(9)	247.79(17)
846	18.4	4.5039(15)	14.039(9)	246.63(17)
847	19.3	4.5006(15)	14.008(9)	245.72(17)
847	19.9	4.4988(15)	13.992(9)	245.25(17)
847	20.9	4.4937(15)	13.955(9)	244.04(17)

772

773

Figure captions

Figure 1.- Observed (black line) and calculated (red line) X-ray diffraction patterns of the calcite-type $Ni_{0.75}Mg_{0.22}Ca_{0.03}CO_3$ gaspeite at room conditions. The green line corresponds to the difference profile between observed and calculated patterns. Vertical magenta marks indicate Bragg reflections.

Figure 2.- (a) Crystal structure of the rhombohedral $R\bar{3}c$ calcite-type $Ni_{0.75}Mg_{0.22}Ca_{0.03}CO_3$. The [$CO_3$] carbonate units and the [(Ni/Mg/Ca)O_6] octahedra are depicted in gray and green, respectively, with the O atoms represented in red. Cell edges are shown as solid black lines. (b) Distorted rocksalt structure of the (Ni,Mg,Ca)C subarray in $Ni_{0.75}Mg_{0.22}Ca_{0.03}CO_3$ (angles ∠C−Ni−C = 65.2°, 76.4º, 103.6º and 114.8º, at room conditions). The solid blue lines would indicate the (Ni,Mg,Ca)−C contacts.

Figure 3.- TGA measurement of $Ni_{0.75}Mg_{0.22}Ca_{0.03}CO_3$ magnesian gaspeite using a 2 °C/min heating rate. The mass loss profile and its first temperature derivative are depicted as black and red solid lines.

Figure 4.- (Top) Raw cake image of the diffraction signal collected in the detector at 1.0 GPa. (Bottom) LeBail fit of the integrated diffraction pattern of the ambient-temperature calcite-type $Ni_{0.75}Mg_{0.22}Ca_{0.03}CO_3$ mineral at this pressure. Observed, calculated and difference X-ray diffraction profiles are depicted in black, red and green, respectively. Magenta vertical marks indicate Bragg reflections. Asterisks (*) denote the diffraction peaks of rhenium, the gasket material.

Figure 5.-XRD patterns at selected pressures using He as pressure-transmitting medium. Asterisks (*) denote the diffraction peaks of rhenium, the gasket material. The plus sign (+) denotes the He(111) diffraction peak.

Figure 6.- Evolution of the unitcell volume of magnesian gaspeite $Ni_{0.75}Mg_{0.22}Ca_{0.03}CO_3$ (experiment, solid squares) and ideal gaspeite $NiCO_3$ (calculations, solid lines) under pressure. RP and HP acronyms come from room pressure and high pressure. Green and red symbols correspond to experimental data of pure $NiCO_3$ and pure $MgCO_3$ magnesite, respectively, from literature data [12, 58]. Dashed lines are the third-order Birch–Murnaghan equation of state fits to the experimental unit cell volume.

Figure 7.- Pressure dependence of the lattice parameters a and c/3 of magnesian gaspeite $Ni_{0.75}Mg_{0.22}Ca_{0.03}CO_3$ (experiment, blue and black solid symbols) and ideal gaspeite $NiCO_3$ (calculations, solid orange line). RP and HP acronyms come from room pressure and high pressure. Green symbols correspond to data for pure $NiCO_3$ reported by Zhang and Reeder [12]. Black solid lines are the third-order Birch–Murnaghan equation of state fits to the lattice parameters.

Figure 8.- Plot of the normalized lattice parameters of $Ni_{0.75}Mg_{0.22}Ca_{0.03}CO_3$ magnesian gaspeite as a function of pressure, which provides the information of axial compressibilities.

Figure 9.- Underlying CsCl-type structure of the (Ni/Mg)C subarray in $Ni_{0.75}Mg_{0.22}Ca_{0.03}CO_3$ magnesian gaspeite at 23.3 GPa.

Figure 10.- Raman spectra of $Ni_{0.75}Mg_{0.22}Ca_{0.03}CO_3$ at different pressures.

Figure 11.- Pressure dependence of the experimentally observed Raman active modes of the calcite-type $Ni_{0.75}Mg_{0.22}Ca_{0.03}CO_3$ magnesian gaspeite.

Figure 12.- Evolution of the theoretical lattice parameters and unit-cell volume of $NiCO_3$ at room pressure (red curves) and 5.5 GPa (blue curves) as a function of temperature.

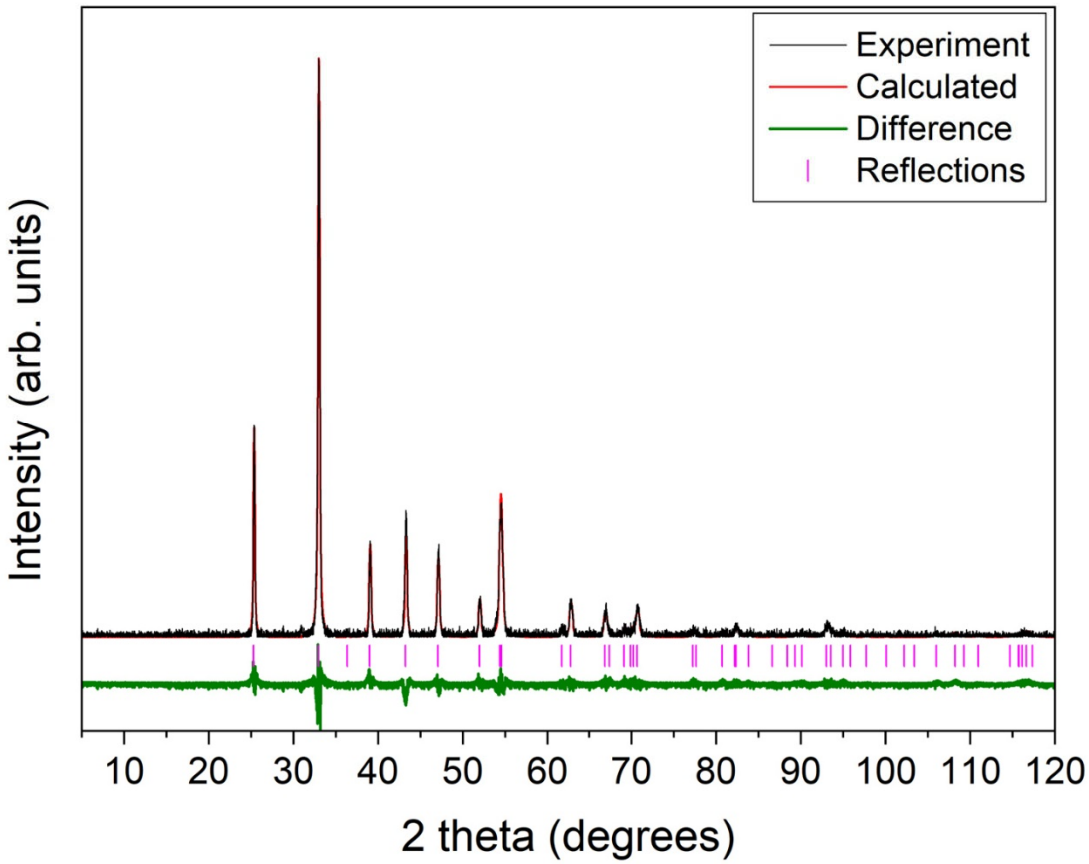
Experiment
Calculated
Difference
Reflections
Intensity (arb. units)
10
20
30
40
50
60
70
80
90
100
110
120
2 theta (degrees)

Figure 1

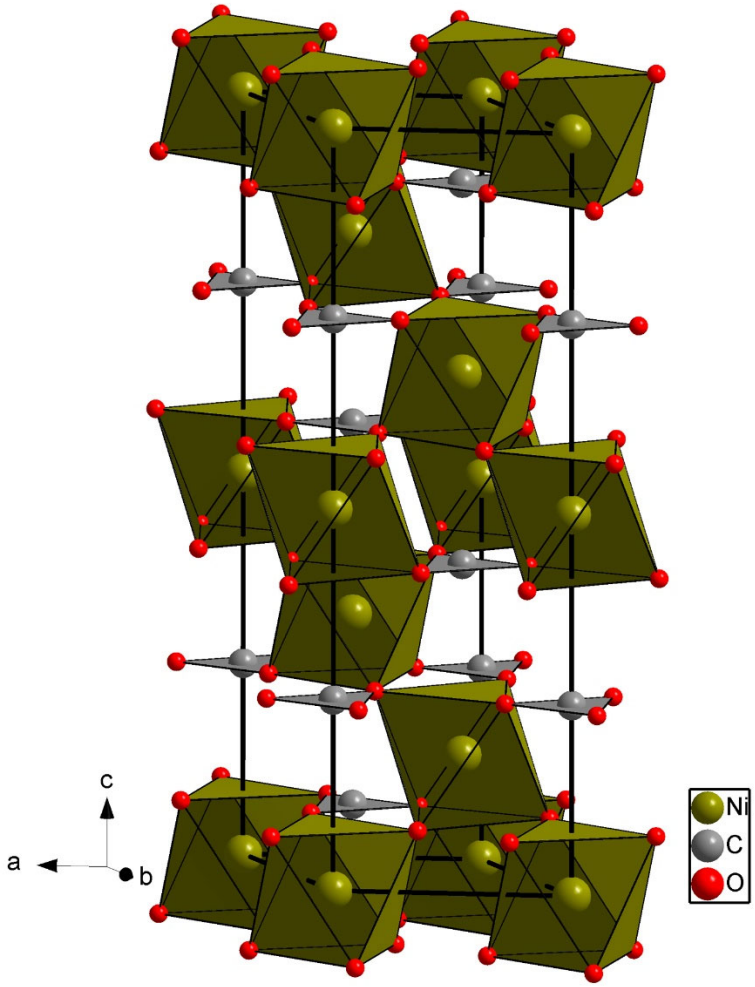

Figure 2a

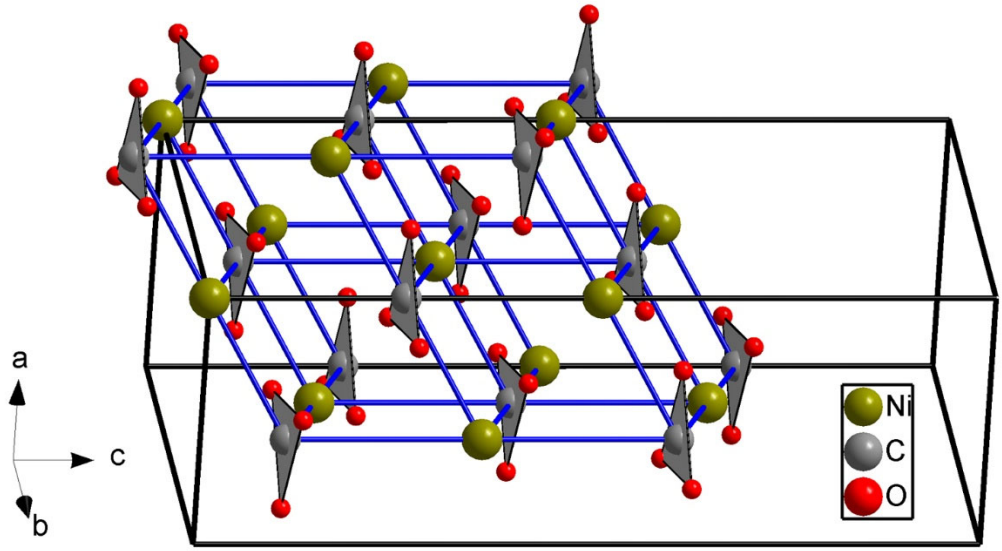

Figure 2b

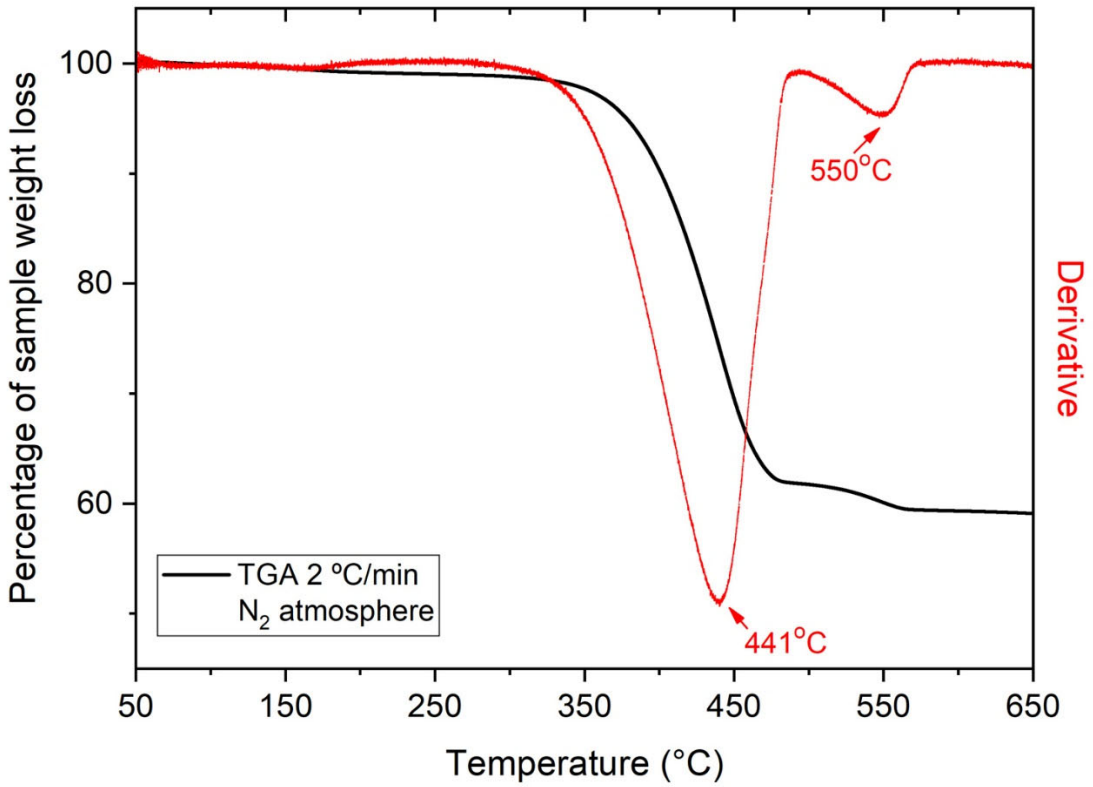
Percentage of sample weight loss
100
80
60
50
150
250
350
450
550
650
Temperature (°C)
Derivative
550°C
441°C
TGA 2 °C/min
N2 atmosphere

Figure 3

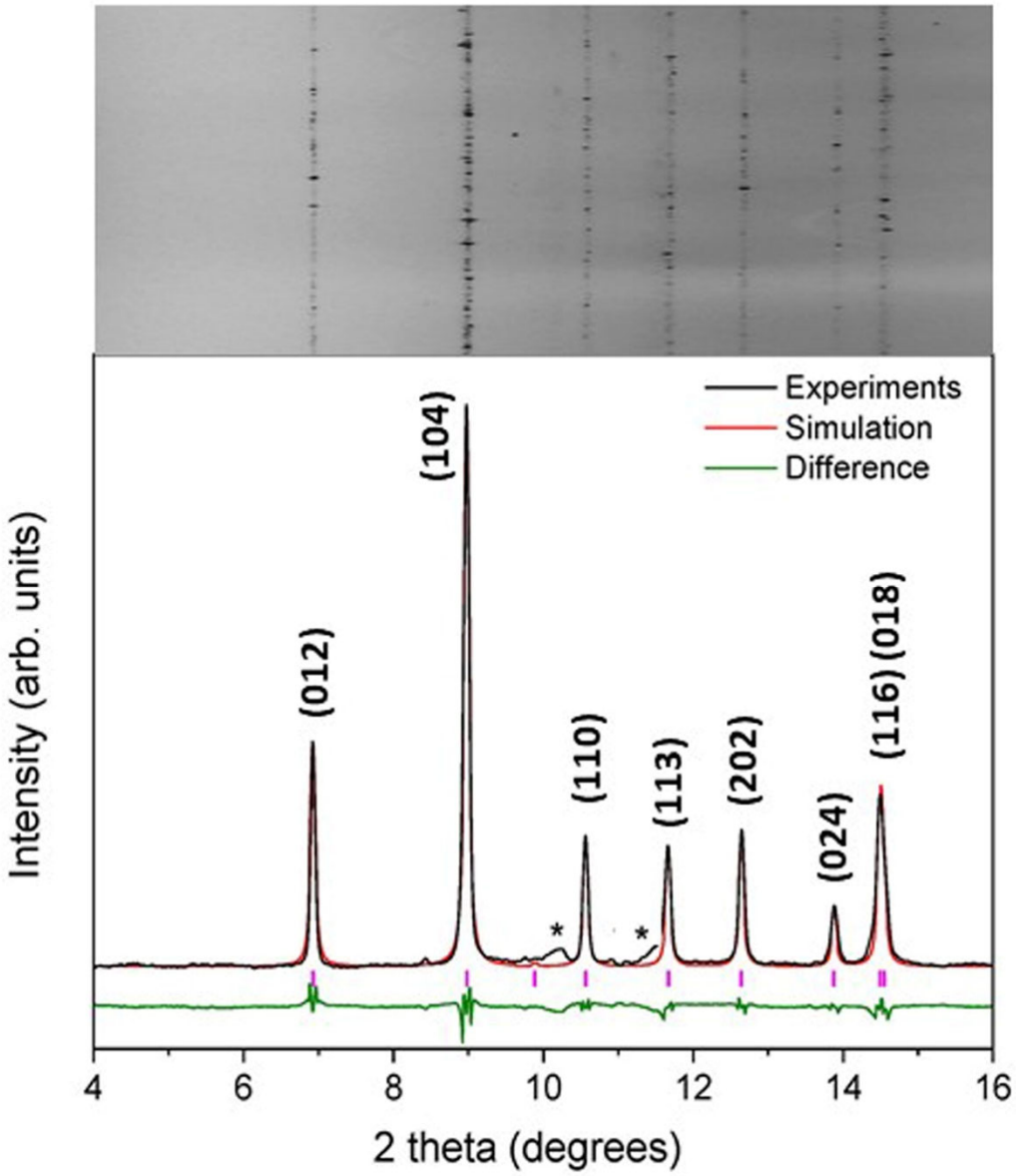
Experiments
Simulation
Difference
(012)
(104)
(110)
(113)
(202)
(024)
(116)
(018)
*
*
Intensity (arb. units)
4
6
8
10
12
14
16
2 theta (degrees)

Figure 4

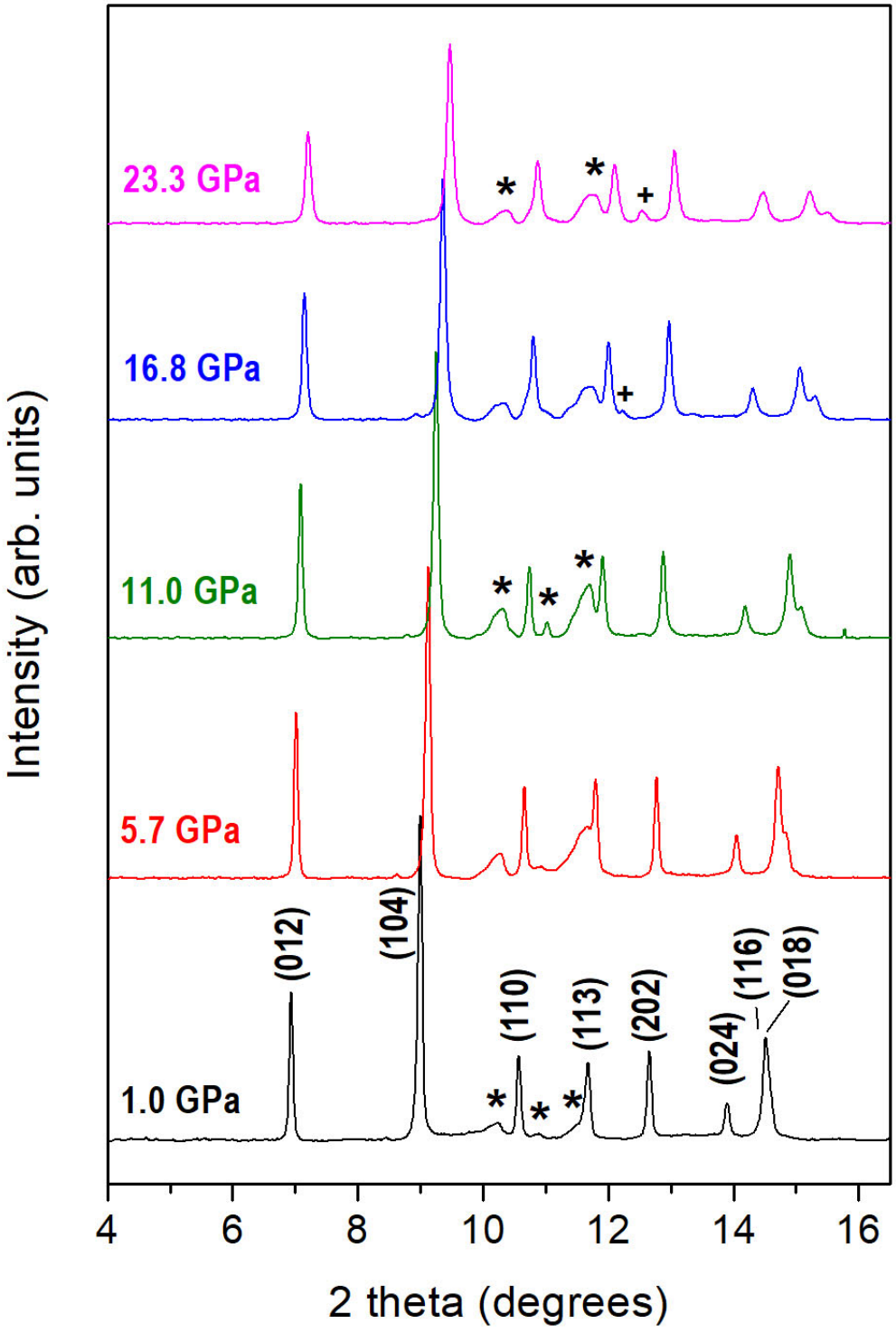

873

874

875 Figure 5

876

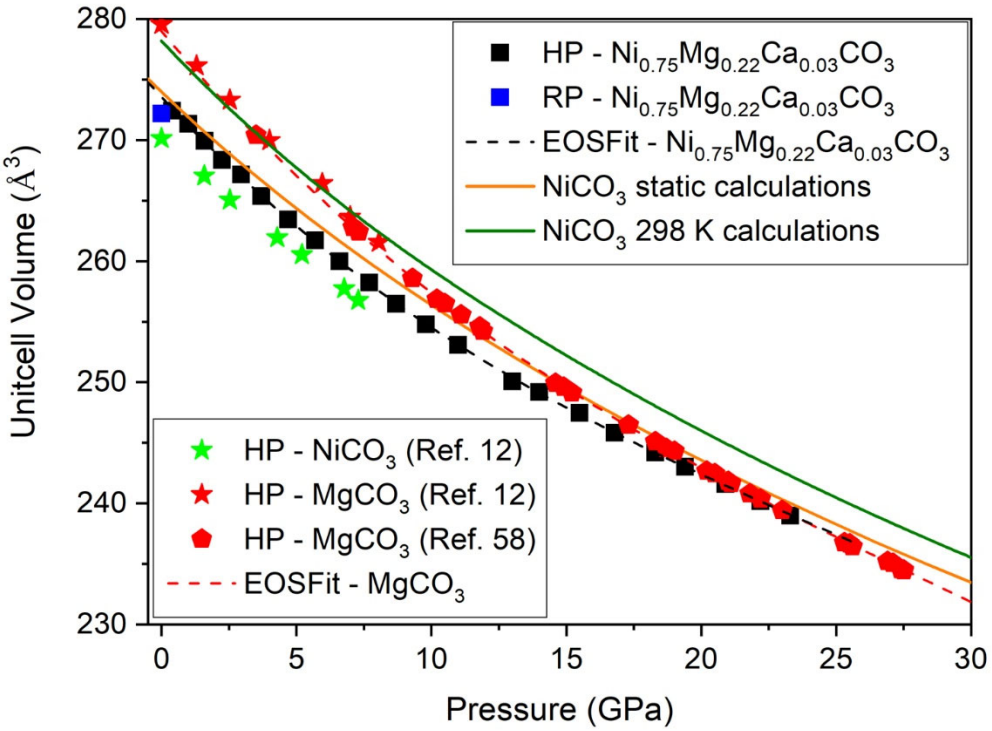
Unitcell Volume (Å^3)
Pressure (GPa)
280
270
260
250
240
230
0
5
10
15
20
25
30
HP - $Ni_{0.75}Mg_{0.22}Ca_{0.03}CO_3$
RP - $Ni_{0.75}Mg_{0.22}Ca_{0.03}CO_3$
EOSFit - $Ni_{0.75}Mg_{0.22}Ca_{0.03}CO_3$
$NiCO_3$ static calculations
$NiCO_3$ 298 K calculations
HP - $NiCO_3$ (Ref. 12)
HP - $MgCO_3$ (Ref. 12)
HP - $MgCO_3$ (Ref. 58)
EOSFit - $MgCO_3$

Figure 6

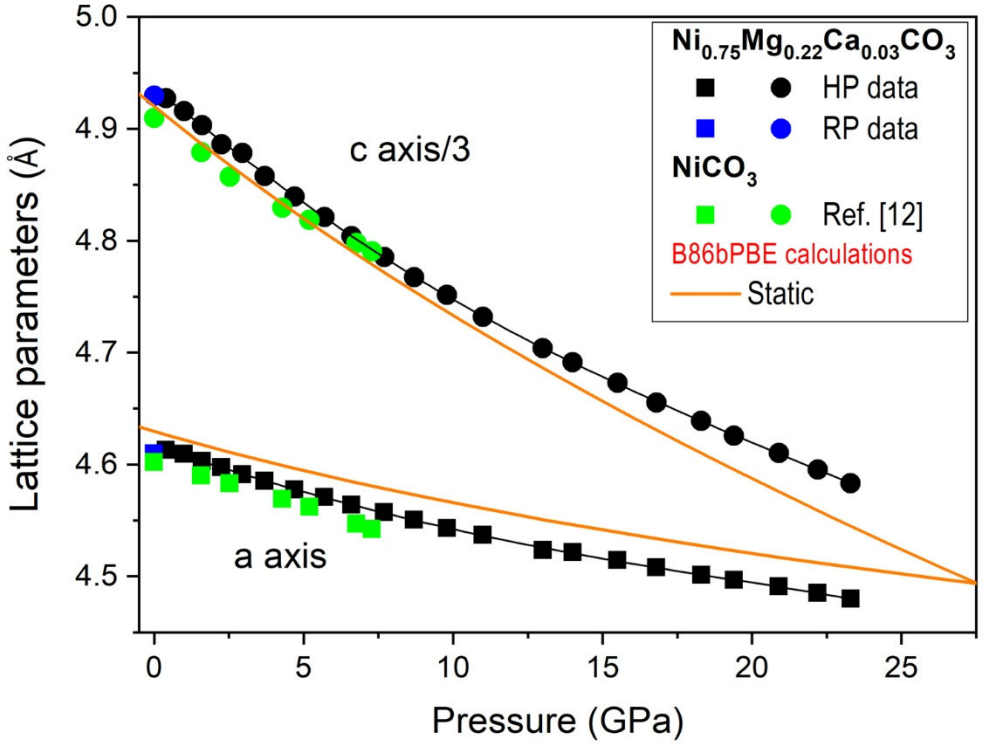
Lattice parameters (Å)
Pressure (GPa)
c axis/3
a axis
Ni0.75Mg0.22Ca0.03CO3
HP data
RP data
NiCO3
Ref. [12]
B86bPBE calculations
Static

Figure 7

892

893

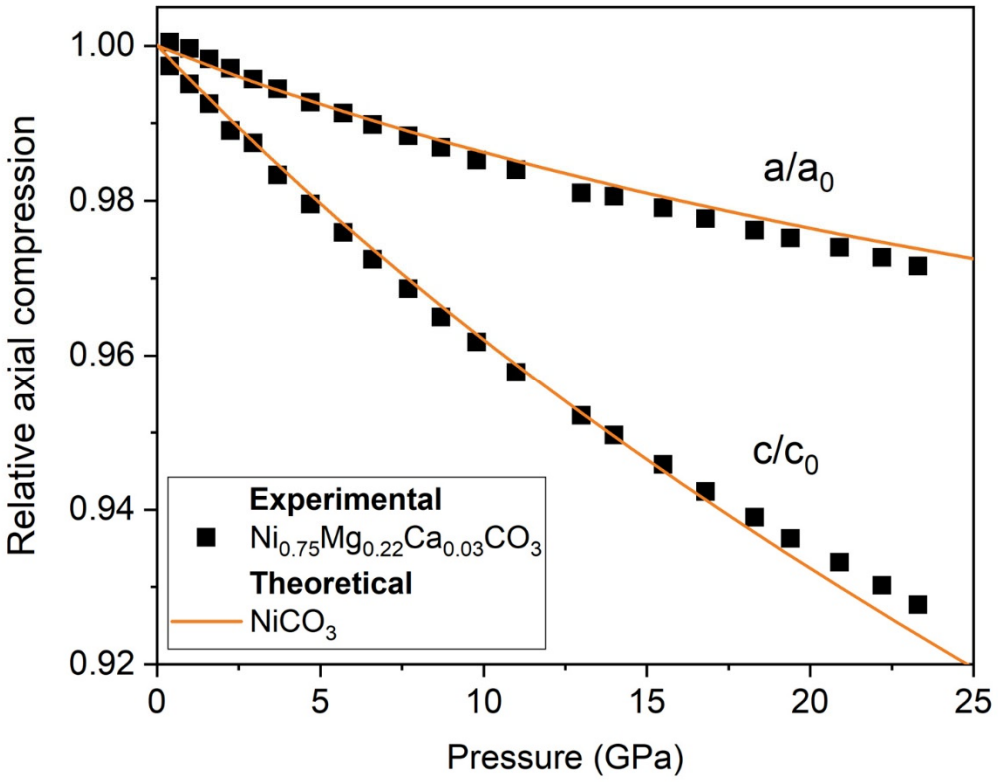

894

895

896 Figure 8

897

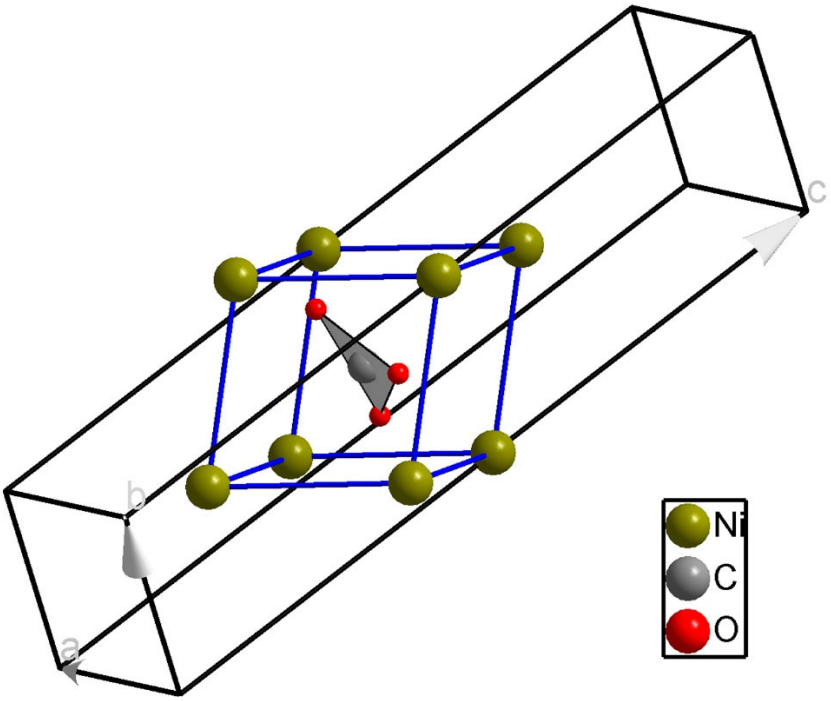

Figure 9

907

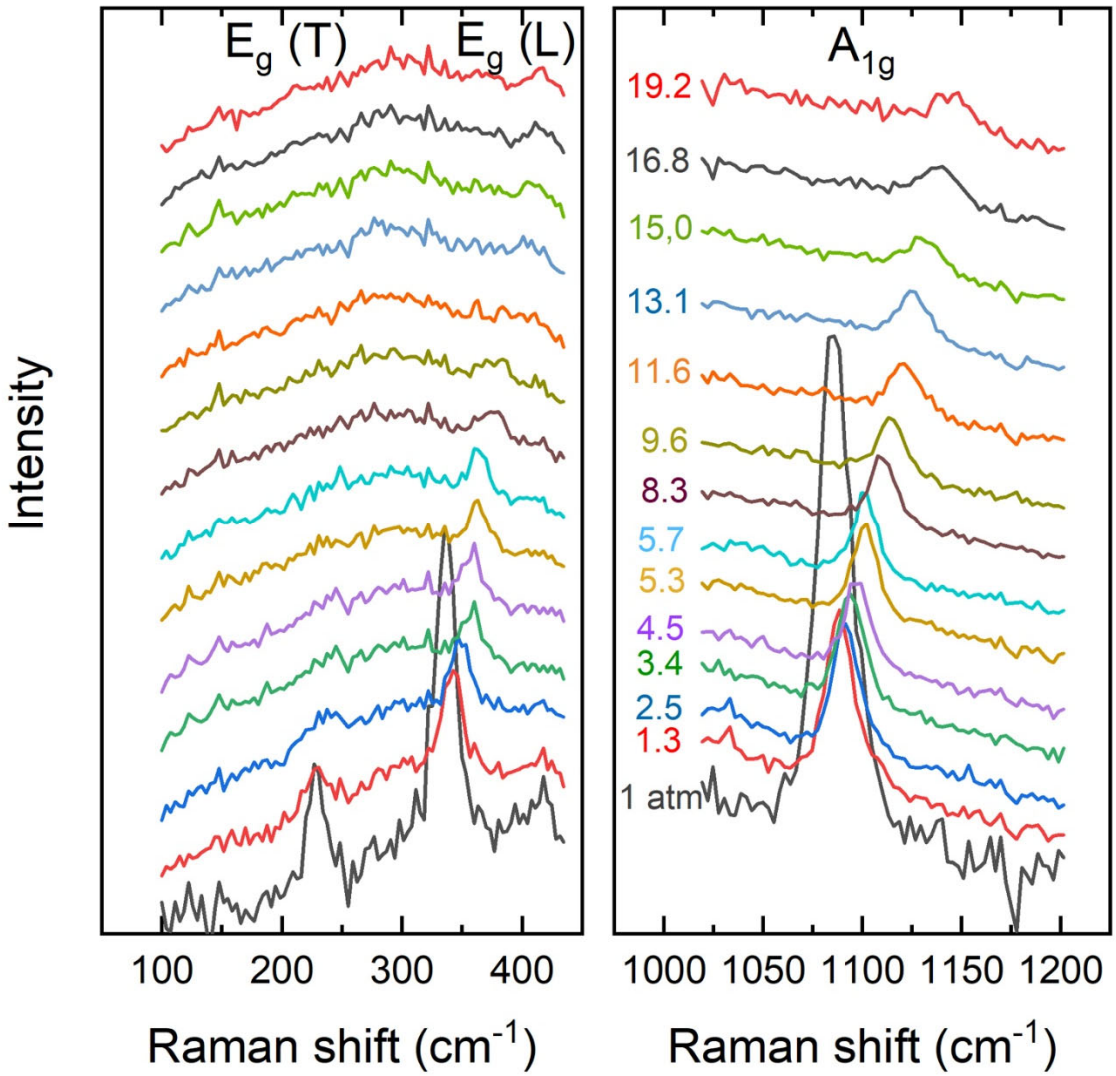

908

909

910 Figure 10

911

912

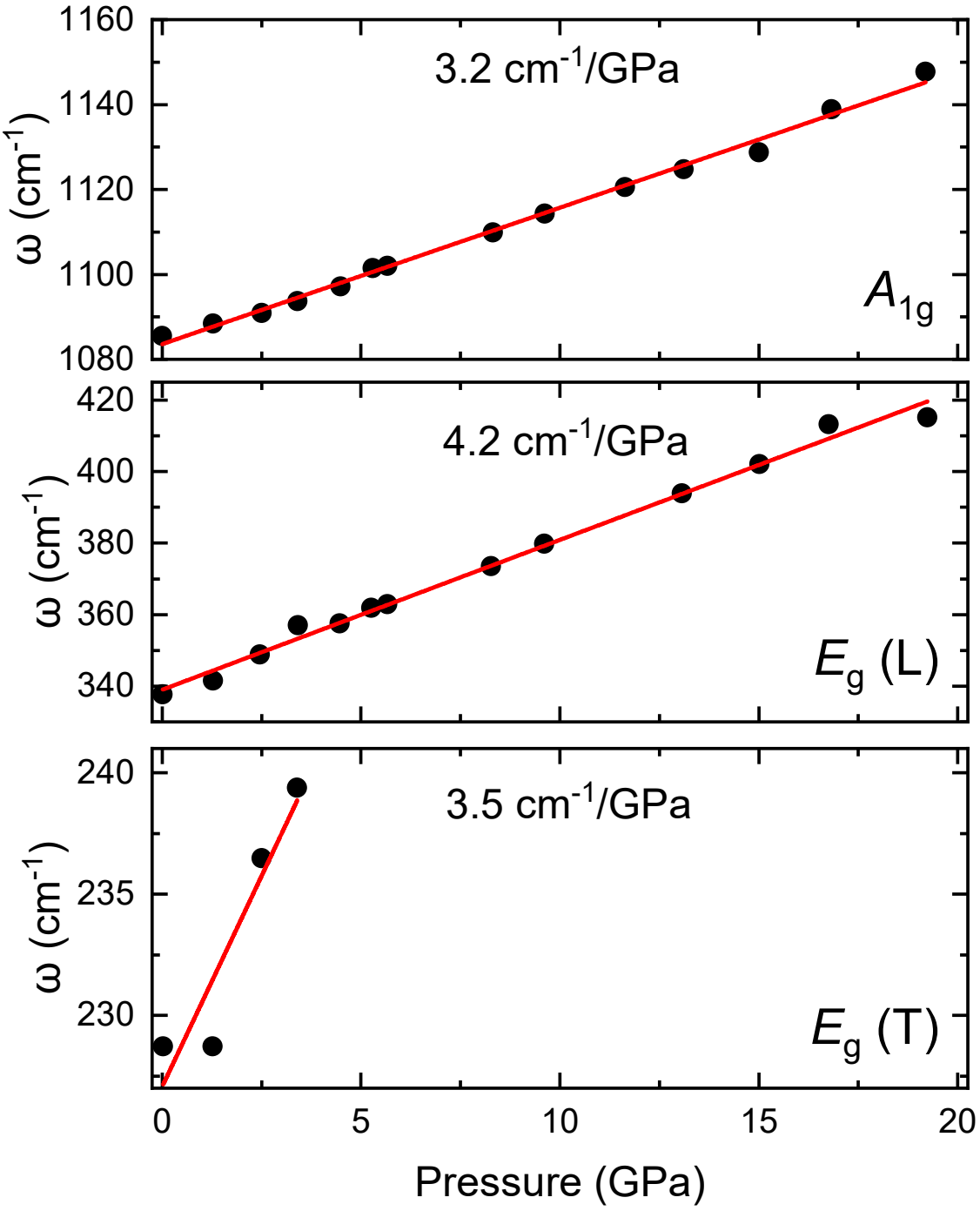

Figure 11

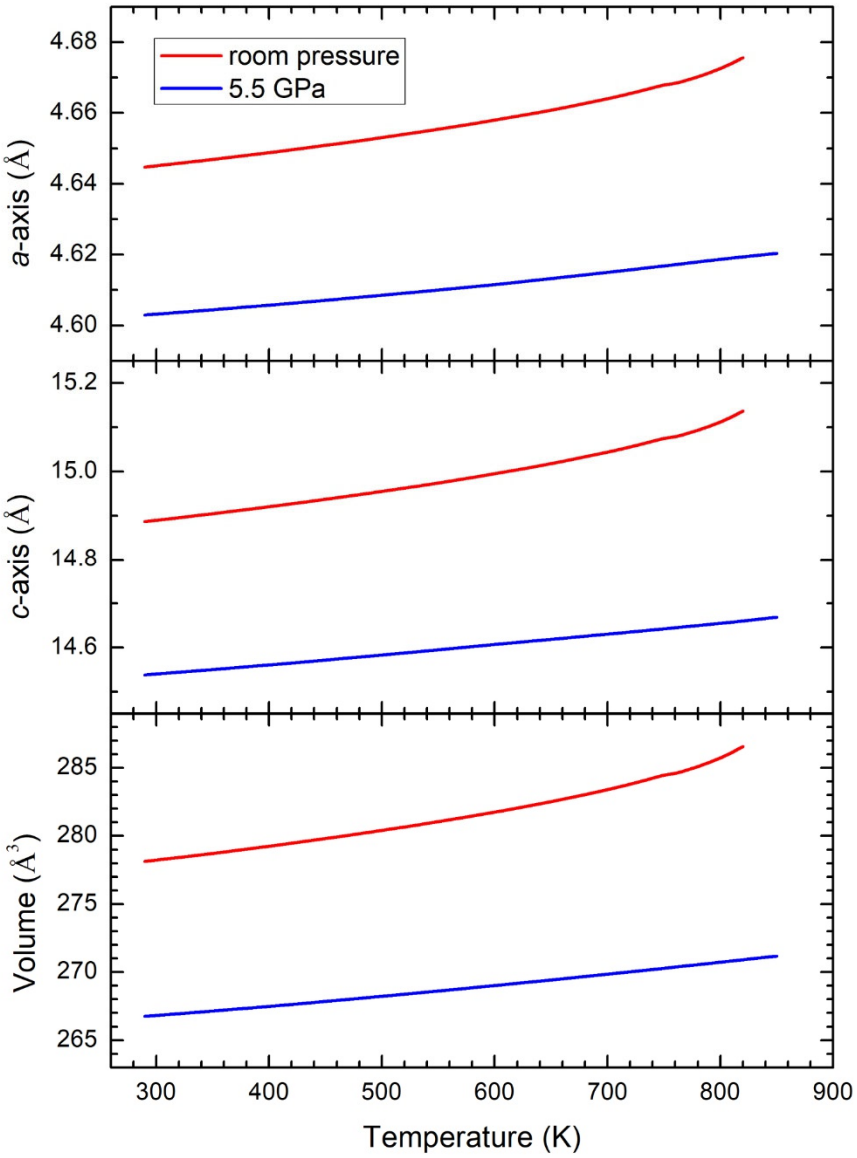
room pressure
5.5 GPa
a-axis (Å)
c-axis (Å)
Volume (Å^3)
Temperature (K)
4.68
4.66
4.64
4.62
4.60
15.2
15.0
14.8
14.6
285
280
275
270
265
300
400
500
600
700
800
900

Figure 12